Atmos. Chem. Phys. Discuss., 15, 26231–26271, 2015
www.atmos-chem-phys-discuss.net/15/26231/2015/
doi:10.5194/acpd-15-26231-2015

Atmospheric Chemistry and Physics Discussions

Transport across the tropical tropopause layer and convection

A.-S. Tissier and B. Legras

Laboratoire de Météorologie Dynamique, UPMC/CNRS/ENS/Ecole Polytechnique, UMR 8539, Paris, France

Received: 2 September 2015 – Accepted: 11 September 2015 – Published: 25 September 2015

Correspondence to: A.-S. Tissier (as.tissier@lmd.ens.fr)

Published by Copernicus Publications on behalf of the European Geosciences Union.

Abstract

Transit properties across the tropical tropopause layer are studied using extensive forward and backward Lagrangian trajectories between cloud tops and the reference surface 380 K. The tropical domain being subdivided into 11 sub-regions according to the distribution of land and convection, we estimate the contribution of each region to the upward mass flux across the 380 K surface, the vertical distribution of convective sources and of transit times over the period 2005–2008. The good agreement between forward and backward statistics is the basis of the results presented here. It is found that about 85 % of the tropical parcels at 380 K originate from convective sources all along the year. From November to April, the sources are dominated by the warm pool which accounts for up to 70 % of the upward flux. During summer, Asian monsoon region is the largest contributor with similar contributions from oceanic regions and Asian mainland, although the signature in vertical distribution and transit time is very different, Asian mainland displaying higher sources and smaller transit times. The Tibetan plateau, although a minor overall contributor, is found to be the region with the highest impact of convection at 380 K due to its central location beneath the Asian upper level anticyclone. We show the robustness of our main results to uncertainties in data and methods but we also find some sensitivity of the vertical distribution of sources and transit times to the representation of cloud tops and heating rates.

1 Introduction

The tropical tropopause layer (TTL) is a key region in the atmosphere that controls the transport of tropospheric air into the stratosphere (Highwood and Hoskins, 1998; Fueglistaler et al., 2009). Situated above the level of main convective outflow (Corti et al., 2006; Fueglistaler et al., 2009), the TTL is penetrated by deep convection which becomes increasingly rare with altitude (Liu and Zipser, 2005; Fu et al., 2007). At the same time, the vertical motion is weak and the region encompasses the level of zero

ACPD
15, 26231–26271, 2015

radiative heating (LZRH) which marks the transition from negative to positive radiative heating values, thus creating a barrier for the large-scale transport of air parcels into the stratosphere (Folkins et al., 1999). Quantifying the transport paths across the TTL, its spatial and temporal variability is important for a better understanding of the chemical composition of the air entering the stratosphere and the relation with source regions (Holton et al., 1995; Fueglistaler et al., 2004; Fu et al., 2006; James et al., 2008; Park et al., 2009; Aschmann et al., 2009; Tzella and Legras, 2011; Bergman et al., 2012; Chen et al., 2012; Bergman et al., 2013; Heath and Fuelberg, 2014; Orbe et al., 2015).

In this work, we focus on how parcels detrained from the convective clouds are transported across the TTL and reach the tropopause, defined as the 380 K surface, upon the combined effect of heating rate fluctuations and vertical distribution of convective sources.

Although the distribution of tropical convection is well known, the location and intensity of convective sources in the TTL are still debated. The questions addressed in this work are whether the intensity is linked only to the altitude of cloud tops (Gettelman et al., 2002, 2009; Devasthale and Fueglistaler, 2010), the role of cloud heating in favoring the crossing of the LZRH (Corti et al., 2006; Tzella and Legras, 2011), the role of horizontal transport and in-mixing from extra-tropical latitudes (Ploeger et al., 2012), and the special role of continental convection during Asian monsoon in particular above the Tibetan Plateau (Fu et al., 2006; Devasthale and Fueglistaler, 2010; Bergman et al., 2013; Heath and Fuelberg, 2014).

We address the whole range of these questions by performing for the first time a comprehensive set of forward and backward trajectories in the TTL between convective sources and the tropopause. We do not account for the transport from the boundary layer to convective tops which is assumed to be fast and local.

In Sect. 2, we describe the data and the methods used in this work to retrieve trajectories connecting the clouds and the 380 K potential temperature surface. Section 3 discusses the distribution of convective sources and transit times in the TTL. Section 4 discusses the sensitivity of our results t uncertainties in the data and methods. Sec-

ACPD
15, 26231–26271, 2015

tion 5 makes a further step by calculating the mass flux across the 380 K surface and the contributions of convective sources. Section 6 offers a summary and outlook.

2 Lagrangian trajectories and convective sources

Lagrangian trajectories of air parcels are calculated within the TTL between the time of detrainment from convective sources and the crossing of the 380 K potential temperature surface, taken as the lower boundary of the stratospheric over-world Holton et al. (1995).

2.1 Determination of the altitude of deep convective clouds

A prerequisite of this study is a characterization of cloud tops that is both global in space and time. We use the CLAUS dataset (Hodges et al., 2000) which provides global 3-hourly maps of brightness temperature at 30 km resolution, combined with ERA-Interim data (Dee et al., 2011) to determine the pressure of the top of the convective clouds. Since we are only interested by air parcels which are able to reach the LZRH and above, we consider only cold pixels with brightness temperatures less than 230 K. In the deep tropics between 15° S and 15° N, this temperature corresponds to a pressure of about 240 hPa which is below the main detrainment level near 200 hPa and well below the all-sky LZRH which is usually located above 155 hPa. As the mean detrainment levels and the LZRH are even higher over continents and in particular over Asia during monsoon season, this is a very conservative choice.

This method is, however, limited by the inability to distinguish overlaying cirrus from convective tops and is known to underestimate the altitude of the deep convective clouds by about 1 km (Sherwood et al., 2004; Minnis et al., 2008). We correct the altitude provided by CLAUS by an upward shift of 1 km. The sensitivity to this correction is described in Sect. 4.1. An other limitation is that the brightness temperature can be colder than the environment and sometimes is colder than the cold point tropopause.

ACPD
15, 26231–26271, 2015

This is possible under fast adiabatic cooling within active convective towers (Adler and Mack, 1986; Luo et al., 2008) and is found to occur for less than 2 % of the cold pixels for each month in the 20° S–40° N band. In such cases, we follow Sherwood et al. (2004) and consider that the parcels rise adiabatically from an altitude of about 40 hPa below the cold point tropopause.

2.2 Three dimensional Lagrangian trajectories

We compute forward and backward diabatic three-dimensional trajectories in the TTL using TRACZILLA, which is a modified version of FLEXPART (Stohl et al., 2005; Pisso and Legras, 2008). The horizontal part of the motion is calculated using the 3-hourly wind fields of ERA-Interim (Dee et al., 2011), combining analysis at 00:00, 06:00, 12:00 and 18:00 UT, 3 h forecast at 03:00 and 15:00 UT and 9 h forecast at 09:00 and 21:00 UT. The vertical (cross-isentropic) displacement is calculated using the 3-hourly average all-sky radiative heating rates of ERA-Interim (including the radiative effect of the clouds but excluding the latent heating) which are archived at 01:30, 04:30, 07:30, 10:30, 13:30, 16:30, 19:30 and 22:30 UT.

The forward calculation are meant to estimate the impact and efficiency of convective sources while the backward calculations estimate the contribution of sources to the air composition at the 380 K surface. The two calculations provide, however, very consistent results as shown below. The calculations are performed over the whole period 2005–2008 and are discussed below in terms of monthly statistics.

2.2.1 Backward simulation

In the backward calculation, parcels are launched from the 380 K potential temperature surface, every two days, between 40° S and 40° N, on a regular grid of 0.5 degree in latitude and longitude. We retain the first encounter of a parcel with the top of a cold cloud within the previous three months as in Tzella and Legras (2011) except that our criterion is based on pressure rather than temperature. A parcel encounters a

ACPD
15, 26231–26271, 2015

cloud when its pressure is larger than the pressure of the corrected top as described above. The comparison is performed 3-hourly along the trajectory of the parcel with the CLAUS pixel containing the parcel at that time. It is clear that we may miss some cloud encounters in this way because the parcels can sometimes travel by 300 km or more over 3 h, that is 10 CLAUS pixel sizes, under strong wind conditions. The sensitivity to such effect is tested in Sect. 4.2

2.2.2 Forward simulation

In the forward calculation, parcels are launched from 3-hourly CLAUS maps, with one parcel at the center of each cold pixel (brightness temperature ≤ 230 K) at the corrected altitude of the cloud top, for locations between 20° S and 40° N. Trajectories are integrated for three months and we retain the first crossing of the 380 K surface between 40° S and 40° N when it occurs. Parcels encountering other clouds along their path, that is which are found within cloudy pixels with cloud tops higher than their altitude, are discarded. On the average, between 16 % (January) and 24 % (August) of the launched parcels are ending their flight in this way. Such parcels are mostly on a descending path and keeping them instead of discarding them affects only marginally our results for parcels crossing the 380 K surface.

3 Source distribution

We focus our study on different geographical regions as defined by the color boxes on Fig. 1. The boundaries are chosen to highlight the regions where convection is intense in the tropics and subtropics and to separate land and oceanic contributions. The South Asian Pacific (SAP) region corresponds to the warm-pool. The Asian monsoon region is divided into the continental Asia Mainland (AML), the North Asian-Pacific Ocean (NAPO) which includes the Bay of Bengal and the Sea of China and the Tibet defined

ACPD
15, 26231–26271, 2015

as the region in Asia above 3500 m. America is divided into South America (SAm) and Central America (CAm). There is a single region for Africa (Af).

3.1 Annual cycle

The black curve in Fig. 2a shows that on the average 86 % of the backward parcels reach a cloud top within three months. The time axis for this curve is the launch time. The parcels which do not reach a cloud are to a vast majority initialized in the subtropics and ascend backward in the deep Brewer-Dobson circulation of the extra-tropics. The proportion of parcels reaching a cloud varies very little over the mean annual cycle with a maximum in April (88.7 %) and a minimum in July (84.7 %).

The other curves in the same panel show the contributions of each region among the trajectories reaching a cloud within the ensemble of all regions in Fig. 1. In order to facilitate the comparison with forward calculations, the time axis for these curves is that of the intersection of each parcel with a cloud, grouped by months.

The main feature between November and April is the domination of the SAP region which accounts alone for a maximum of 68.4 % of all sources in January. The next winter contributors are Af and SAm with a maximum contribution of 19.4 % for Africa in April.

From June to September, NAPO dominates with a maximum share of 35.3 % in July followed by AML which caps at 19.8 % in July. Together these two regions represent from 45 to 55 % of all sources from June to September. The following contributors are SAP, CAm, North Central Pacific (NCP) and Af. Tibet is a tiny overall contributor (with is maximum share of 2.5 % in July).

The forward estimate of the source distribution, see Fig. 2b, is calculated from the trajectories launched at cloud top level which have reached the 380 K surface. The quantity shown is the monthly ratio of the number of parcels from a given region to the total number originating from the ensemble of regions in Fig. 1. The time associated with each trajectory is that of its launch, grouped into monthly bins. There is a striking agreement between the forward and backward distribution of sources in Fig. 2a and 2b.

ACPD
15, 26231–26271, 2015

In spite of some slight quantitative changes in the proportions, the general pattern and the ordering of sources is quasi-identical over the whole year. The largest change is for Tibet which displays a forward contribution of 7.6 % in July and August, that is three times its backward contribution but still remains a minor overall contributor.

The similarity is not totally unexpected as forward and backward calculations are solving dual equations for the Green function of the advection-diffusion equation (Holzer and Hall, 2000; Legras et al., 2005). Here diffusion has no role because we consider averages over regions and durations much larger than the diffusion scale and time as defined in Legras et al. (2005). It is however surprising that a somewhat coarse discretization (only one parcel per cold 30 km × 30 km pixel in the forward case and one parcel on a half-degree grid every two days) which under-samples quite drastically the flow is able to reach good agreement between forward and backward calculations. The sampling is made at a higher resolution than the ERA-Interim winds but the transit time between the cloud top and the 380 K surface is long enough (as shown below) to make the trajectories numerically irreversible due to the transport chaos. Our results show that the sampling is good enough to reestablish the reversibility in the statistical sense as predicted by the Green function formalism for a continuous sampling (Holzer and Hall, 2000).

Figure 2c shows the proportion of forward trajectories released in a given region from high convective tops that reach the 380 K surface within 3 months. As most of the other trajectories have returned back in the lower troposphere, this proportion conveys the efficiency of each region at converting convective air into stratospheric air. Tibet displays a singular behaviour by reaching an efficiency of 84.5 % in July which indicates that this proportion of air detrained at the top of clouds reaches the 380 K surface. During summer, after Tibet, AML conveys up to 53.5 % of parcels to the stratosphere while NAPO is less efficient at about 32.5 % but still the largest contributor due to its size and the frequency of high convective clouds within its domain.

The other regions exhibit efficiency lower than 30 % with SAP lying above SAm, CAm and Af. However, when the Asian land convection fades in, the larger efficiency of SAP

ACPD
15, 26231–26271, 2015

combines with the intensity of convection in this region to let it dominate the transfers over half of the year.

The high efficiency above Tibet is consistent with previous studies who found a confinement of Tibetan air within the monsoon anticyclone (Bergman et al., 2013; Heath and Fuelberg, 2014) which persists above Asia during summer, trapping tracer compounds that recirculate inside (Park et al., 2007, 2009). The contribution to the inside of the summer Asian monsoon anticyclone (AMA) has been further estimated by calculating sources over the restricted portion of the 380 K surface confined between 20 and 40° N, 25 and 125° E, and with potential vorticity smaller than 4×10^6 m^2 s^{-1} kg^{-1} K. It is found that 87 % of the AMA parcels originate from Asia in the forward calculation, see Fig. 2b, among which 19,5 % from the Tibetan plateau. In the backward calculations, see Fig. 2a, the proportions are redistributed among Asian continental convection between AML and Tibet (respectively 47.5 and 19.5 % in forward and 54.3 and 8.8 % in backward, the sum varying only from 67 to 63.1 %). The NAPO contribution is unchanged.

3.2 Vertical distribution of sources

We investigate now the vertical distribution of sources within each region and its relation with the LZRH. During winter, see Fig. 3a and 3b, forward and backward calculations predict that the distribution of cloud top sources in the dominating SAP region peaks at 355 K, that is above the all-sky LZRH located at 352.6 K during that season. A proportion of 89.5 % of the sources are then located above the LZRH in the forward calculation and 76.3 % in the backward calculation. The other contributing regions (Af, SAm, NAPO and NCP) also exhibit all a modal peak at 355 K in the forward distribution. The backward distribution exhibits a shift towards small potential temperature which affects also the mean and the median of the distribution (see Table 1).

As in Tzella and Legras (2011), a more complex pattern emerges during summer with several competing regions, see Fig. 3c and d. Both forward and backward calculations produce similar distribution of sources with the main differences being a stronger

ACPD
15, 26231–26271, 2015

contribution of Asian land regions (AML and Tibet) in the forward distribution. SAP, CAm and NCP regions are grouped in the forward calculation with a modal peak at 353 K which is below the winter peak at 355 K in SAP. A similar pattern is found in the backward calculation. The AML and Tibet modal peaks are above 360 K, reaching 367 K for Tibet. Africa modal peak is also near 360 K with a fairly flat distribution, and NAPO modal peak is intermediate near the common winter peak. The backward shift in the sources towards small potential temperature is smaller than during winter in SAP. Most of the sources are again located above the LZRH, up to 90 % for the forward trajectories from NAPO and CAm (see Table 1). The only exception is Tibet, for which the LZRH, much higher than in other regions at 367.3 K, is located above the modal peak, and just at the median in forward calculations. Nevertheless, Tibet was found quite paradoxically as the region with highest efficiency during summer. The separation of NAPO and Asian land sources explain the double peak pattern shown in Fig. 8 of Tzella and Legras (2011).

3.3 Transit time

The differences between forward and backward calculations are mostly seen in the transit time distribution shown in Fig. 4. The peak of the distribution is always shifted to smaller values in the forward calculations and the tail is also decaying much faster. As a result, the ratio backward/forward for the median and the mean is of the order of 1.5 in SAP during winter and in AML and NAPO during summer. It is lower but always larger than 1.1 in the other regions with the exception of Tibet with a near 2 factor, see Table 2. In the forward calculation, the mean transit time over contributing oceanic regions (SAP, NCP and CAm) is of the order of 30 days during summer, which is larger than the winter value of 23 days in SAP. On the contrary, Asian land regions during summer exhibit shorter transit times (21 days for AML and 15 days for Tibet) than their winter counterparts (Af and SAm) near 28 days. Af shows very little change between winter and summer.

ACPD
15, 26231–26271, 2015

The backward distribution is biased by the fact that sampled backward trajectories can easily miss a cloud by passing a pixel away and then wander away in another region. The effect is the largest for small regions like Tibet or regions ventilated by large scale intense circulation such as Asia during summer. The backward trajectories can also, at least in principle, get trapped into unstable trajectories oscillating about the LZRH from which trajectories diverge in forward time and to which they therefore converge in backward time, although this has seldom been observed. As it appears, transit times are more sensitive to sampling effects than the source distribution.

4 Sensitivity studies

In this section, we study the sensitivity of the results presented in Sect. 3 to changes in data and the design of our calculations.

4.1 Sensitivity to the cloud top offset

As the estimate of cloud top and the +1 km correction are subject to uncertainty, we have redone the analysis without the +1 km correction. Since the LZRH is the same, the direct effect is to reduce the proportion of forward trajectories reaching the 380 K surface, see Table 3. The ratio is about 45 % for both summer and winter but for continental Asia during summer where it is smaller. Tibet is the most sensitive region with a ratio of 22 %.

Figures 5a and 5c shows the change in the vertical distribution of sources for forward calculations. Besides the overall reduction, it is visible that the modal peaks are unmoved but for NAPO and Tibet during summer where they move, respectively, from 358 to 355 K and from 367 to 362 K. The vertical distribution of sources is made narrower by reducing the aisle of the distribution towards the upper end of the interval as the highest clouds are shifted down.

ACPD
15, 26231–26271, 2015

The proportion of backward trajectories reaching a cloud within 3 months is now 85 % during DJF and 82.7 % during JJA, that is less but close to the value when the offset is applied (87 and 85.2 % respectively), hence with much less variations than the forward efficiency. The modal peaks are slightly shifted to lower values (with larger shift for NAPO and Tibet) and the narrowing is well pronounced with almost no sources within the [365, 370 K] except over continental Asia during summer.

The lower end cutoff value of sources (at about 345 K for maritime convection and 350 K for AML) is preserved in both forward and backward calculations but for Tibet. This suggest that this cutoff is determined by the transport properties across the LZRH which are unchanged by offsetting the cloud top while the cutoff above the LZRH depends strongly on the distribution of cloud tops. Tibet differs by being the only region where the LZRH is above the modal peak.

Accordingly to these limited changes in the sources, the transit time distribution for all regions but Tibet is weakly affected for both forward and backward calculation, see Fig. 6. The change is localized in the small time contribution in agreement with the narrowing of the source distribution which reduces the proportion of short transit paths. Tibet is an exception with a shift by about a factor two of the forward and backward transit times towards larger values. Tibet differs from the other regions by having a very high LZRH and a distribution of sources laying mainly under this level. This effect is amplified when the cloud top correction is cancelled with almost no contribution left above the LZRH, inducing a significant shift in the transit time distribution.

4.2 Sensitivity to increase of the size of cloud pixels

In this section we address the sensitivity to the density of cloud observation and the effect of missing cloud encounters in backward calculations. We modify the encounter criterion by enlarging the pixel size by a factor three in both latitude and longitude, retaining the smallest top pressure among the 9 CLAUS pixels surrounding the parcel at a given time. This modification enlarge high clouds and has largest effect in regions where convective systems are small and sparse. Figure 7 compares the distribution of

ACPD
15, 26231–26271, 2015

backward sources in winter and summer 2005 with and without enlarging the pixel size. The total number of trajectories meeting a cloud is again quite insensitive increasing by 3 % during winter and 1.5 % during summer. The distribution of sources is however modified by shifting the distribution to higher potential temperatures and widening the profile. Hence, the effect is quite opposite, qualitatively to the lowering the top of clouds done in Sect. 4.1.

4.3 Sensitivity to the reanalysis

One main source of uncertainty is the error in the reanalysis wind and heating rates. It has been shown that the heating rates differ quite significantly among reanalysis (Wright and Fueglistaler, 2013) and that the horizontal wind may be quite erroneous in tropical regions poorly covered by radio-soundings (Podglajen et al., 2014). It is therefore important to assess how our results are sensitive to a change of the reanalysis. As an extensive comparison among all available reanalysis at the time of this writing would have consumed a lot of resources, we limit the comparison to the JRA-55 (Kobayashi et al., 2015) which has higher horizontal resolution than the ERA-Interim (spherical T319 truncature instead of T255) and the same number of levels. Winds and heating rates are available every 6 h at model resolution.

Backward calculations have been performed for 2005 using the same setup as for ERA-Interim. The vertical source distribution shown in Fig. 8 is to be compared with the two upper panels of Fig. 7. There is very good qualitative agreement but there are also differences. SAP is even more prominent during winter and but the largest difference is in NAPO taking a larger share during summer. The distributions are also shifted towards higher altitudes, a result which is compatible with a generally higher LZRH in JRA-55 (not shown). The total proportion of backward trajectories meeting a cloud remains, however, very close to that of the ERA-Interim (81 % against 85 % in 2005).

ACPD
15, 26231–26271, 2015

5 Mass flux across the 380 K surface and regional distribution

In this section, we make a further step by determining the mass flux across the 380 K surface and the contribution of each convective region.

5.1 Method and validation

The instantaneous diabatic mass flux M across the 380 K surface, over a specific domain Γ of the sphere, can be estimated from all sky radiative heating rates as:

$$M_{\text{diab}} = \iint_{\Gamma} \sigma_{380\,\text{K}} \left.\frac{\mathrm{d}\theta}{\mathrm{d}t}\right|_{380\,\text{K}} \mathrm{d}s, \tag{1}$$

with $\sigma_{380\,\text{K}} = -\frac{1}{g}\frac{\partial p}{\partial \theta}$ at $\theta = 380\,\text{K}$, obtained from the temperature and pressure profile of ERA-Interim, with $g = 9.81\,\text{m}\,\text{s}^{-2}$. For practical purposes, the integration is replaced by a weighted sum over the gridded surface. From these instantaneous fluxes, one can define monthly averages by replacing $\left.\frac{\mathrm{d}\theta}{\mathrm{d}t}\right|_{380\,\text{K}}$ in Eq. (1) by its monthly average $\left\langle \left.\frac{\mathrm{d}\theta}{\mathrm{d}t}\right|_{380\text{K}} \right\rangle$. The monthly upward $M^{\uparrow}_{\text{diab}}$ and downward $M^{\downarrow}_{\text{diab}}(\phi)$ fluxes can then defined be integrating separately on the sub-domains where $\left\langle \left.\frac{\mathrm{d}\theta}{\mathrm{d}t}\right|_{380\,\text{K}} \right\rangle$ is, respectively, positive and negative. It is known that upward and backward fluxes are ill-defined when the time interval goes to zero (Hall and Holzer, 2003). This is no longer the case after time smoothing which removes the noise but the flux then may depend on the applied time smoothing interval.

ACPD
15, 26231–26271, 2015

Another, mode traditional, method is based on the residual mean meridional circulation $\left(\overline{v^*}, \overline{w^*}\right)$, with

$$\overline{v^*} = \overline{v} - \frac{1}{p}\frac{\partial}{\partial z}\left(p\frac{\overline{v'\theta'}}{\overline{\theta}_z}\right) \tag{2}$$

$$\overline{w^*} = \overline{w} + \frac{1}{a\cos\phi}\frac{\partial}{\partial \phi}\left(\cos\phi\frac{\overline{v'\theta'}}{\overline{\theta}_z}\right) \tag{3}$$

as defined by Andrews et al. (1987) in log pressure coordinates $z = H\log(p_0/p)$ where the bars stands for the zonal average. This kinematic mass flux is then given by (Appenzeller et al., 1996):

$$M_{\text{kine}} = \iint\left[\frac{p_{380\,\text{K}}}{gH}\left(\overline{w^*} - \frac{1}{a}\frac{\partial z}{\partial \phi}\bigg|_{380\,\text{K}}\overline{v^*}\right) + \frac{1}{g}\frac{\partial p}{\partial t}\bigg|_{380\,\text{K}}\right]\mathrm{d}s, \tag{4}$$

with $p_{380\,\text{K}}$ the pressure at the 380 K surface, $a = 6371$ km and $H = 7$ km. Monthly upward and downward fluxes, $M^{\uparrow}_{\text{kine}}$ and $M^{\downarrow}_{\text{kine}}$, can be separated according to the sign of the monthly average term under the integral (Eq. 4). Gridded summation is applied in the same way as M_{diab}.

Figure 9 compares the monthly average upward fluxes calculated from (Fig. 1) and (Fig. 4). Here the diabatic flux is calculated from 3-hourly data and then averaged for each month over the period 2005–2008. The upward flux is calculated as indicated above for each month and then average over the four years. The kinematic mass flux is calculated in the same way from monthly averages of the residual circulation and pressure at 380 K. The contribution of the pressure variation term in (Fig. 4) is then two orders of magnitude smaller than that of the residual velocity and can be neglected.

The two estimates display a similar modulation with a minimum during summer and agree with other estimates from the ERA-Interim (Abalos et al., 2012). There is, however, a shift between $M^{\uparrow}_{\text{diab}}$ and $M^{\uparrow}_{\text{kine}}$ which increases with the size of the latitude band.

ACPD
15, 26231–26271, 2015

The mean difference is close to 25 % in the three latitude bands. It is noticeable that the upward flux and the total flux are identical in the 20° S–20° N band because this domain of the surface 380K is heated everywhere all along the year in monthly average. It is also noticeable that there is little change in the upward flux between 30° S–30° N and 40° S–40° N because most of the upward motion occurs within the former band.

The discrepancy between diabatic and kinematic fluxes can be reduced by correcting the diabatic mass flux to satisfy global mass conservation. There is no physical mean to constrain such mass conservation when calculating heating rates (Shine, 1989) from radiative transfers and actually the mean total mass flux across the 380 K provided by Eq. (1) and the ERA-Interim data is $7.9 \times 10^9\,\mathrm{kg\,s^{-1}}$ over 2005–2008. Applying a uniform compensating correction to the heating rates over the sphere defines a new mass flux $M^{\uparrow}_{\mathrm{diab,corr}}$ which reduces the discrepancy with $M^{\uparrow}_{\mathrm{kine}}$ for all latitudes and all times. However, as this uniform correction is entirely ad hoc in the absence of any information about the spatial and temporal distribution of the errors, we refrain from applying it in the sequel.

The definition used for the diabatic flux is consistent with what follows. However a more appropriate definition to compare with the kinematic fluxes would be to take a zonal average before applying the sign criterion defining the upward flux. The resulting upward flux (not shown) is indeed larger than $M^{\uparrow}_{\mathrm{diab}}$ but the difference in the 40° S–40° N band is of the order of 1 % but in winter where it is less than 2 %. Therefore this is taken as negligible and cannot explain the shift between kinematic and diabatic fluxes.

Notice that the total mass flux across an isentropic surface does not need to vanish instantaneously unlike across an isobaric surface under the hydrostatic approximation. However the small part of the pressure variation term in the monthly flux indicates that the mass balance must be satisfied over monthly averages in the same proportion, that is within about 1 %. This is in agreement with the stratospheric over-world mass variations shown by Appenzeller et al. (1996).

Having compared the diabatic mass flux from heating rates to the kinematic flux, we know check that the diabatic mass flux can also be retrieved from the Lagrangian

ACPD
15, 26231–26271, 2015

trajectories. Here the mass flux is calculated from the displacement of backward Lagrangian trajectories launched at 380 K. The heating rate is estimated as $\Delta\theta/\Delta t$ where $\Delta\theta$ is the variation of the potential temperature along the trajectory during an interval Δt after the launch taken as a multiple of 24 h in order to average over an integer number of daily cycles. The density σ is calculated from the ERA-Interim at the location and time of the launch. Actually, due to combined horizontal and vertical motion, and the inclination of potential temperature surfaces with respect to isobars, pressure can temporarily decrease for a descending parcel with increasing potential temperature. As a general rule, pressure undergoes much larger fluctuations than potential temperature along a Lagrangian trajectory. The mass flux over a domain Γ can then be calculated as a sum over all parcels belonging to this domain

$$M_{\text{back}} = \sum_{i\in\Gamma} \sigma_i \frac{\Delta\theta_i}{\Delta t} \delta s_i \tag{5}$$

where δs_i is the surface of the $0.5 \times 0.5^\circ$ element associated with the parcel. The monthly upward flux $M^{\uparrow}_{\text{back}}(\phi)$ is calculated by averaging over each month the individual parcel flux at each location over the grid, selecting all grid points where the monthly flux is positive and then averaging in longitude.

Figure 10 compares the temporal evolution of $M^{\uparrow}_{\text{diab}}$ and $M^{\uparrow}_{\text{back}}$ over the years 2005 to 2008. It is clear that the Lagrangian estimates with the delays Δt = 24 or 48 h provides an accurate estimate of the upward flux at all latitudes.

5.2 Regional distribution of the upward mass flux

Based on these premises we calculate how the monthly upward flux is distributed among regions in the following way. First the grid point within the domain where the monthly average flux is positive are selected for each month. Then the contributions of parcels originating from a given region is sorted out and the total contribution from this given region is calculated by summing its contributions over all the selected grid points.

ACPD
15, 26231–26271, 2015

The sum of all these regional contributions makes the convective upward flux at the 380 K surface $M^{\uparrow}_{conv}$. In this procedure, a trajectory is labeled with the time of its launch on the 380 K surface (unlike the calculations leading to Fig. 2 where the trajectories where labeled with their arrival or departure from clouds).

Figure 10 shows that $M^{\uparrow}_{conv}$ basically explains the seasonal variations of $M^{\uparrow}_{back}$ with a difference mean of $4.8 \times 10^{9}\,kg\,s^{-1}$ and a standard deviation of $9 \times 10^{8}\,kg\,s^{-1}$ in the 40° S–40° N band . This difference is mostly accounted by parcels which are in-mixed in the TTL from the extra-tropics (Ploeger et al., 2012). The mean annual cycle is shown in Fig. 11. It exhibits a maximum in February and a minimum in September which are shifted by about one month with respect to the maximum and minimum of the source curve in Fig. 2a where the time axis is that of the intersection with convection. The delay is consistent with the distribution of transit time among the main sources (see Table 2).

The larger winter to summer modulation of $M^{\uparrow}_{conv}$ than the total source curve in Fig. 2a suggests that this modulation is mostly due to variations of transport properties within the TTL rather than to a modulation of the properties of convective sources.

Figure 11 shows the same hierarchy among source regions as Fig. 2a with enhanced domination of the SAP contribution over the year which accounts for 39 % of the total $M^{\uparrow}_{conv}$ flux while NAPO accounts for 18 %. If one adds NCP, CAm which is mostly oceanic, and the small contribution from the Atlantic, Indian Ocean and South East Pacific, we see that the contribution from oceanic regions (which include some large islands) is 74.5 % a proportion in pair with the surface covered by the oceans.

We stress that the flux $M^{\uparrow}_{conv}$ is the mass flux crossing the 380 K surface that originates from the region of convective outflow within the TTL but is not necessarily purely made of air processed by convection. This air mass contains convective air detrained from the clouds in the vicinity but is also mixed with environment air which may have been transported from distant and earlier convective sources and partly originates from in mixing or extra-tropical lower stratosphere transported into the tropics (Ploeger et al.,

ACPD
15, 26231–26271, 2015

2012). Therefore $M^{\uparrow}_{\mathrm{conv}}$ must be taken as an upper bound of the flux of convectively processed air.

6 Summary and outlook

We have shown that a consistent vertical distribution of convective sources of stratospheric air over the tropical regions is obtained from backward and forward diabatic trajectories in the TTL.

The seasonal cycle of sources is binary with a domination of the single South Asia Pacific region (SAP) from November to April and a more complicated pattern dominated by the regions of the Asian monsoon from June to September.

The distribution of sources among regions is qualitatively robust to uncertainties in the method and the data but the quantitative distribution is somewhat sensitive to the representation of cloud tops and depend also on the reanalysis. Generally, increasing the weight of highest clouds shifts the distribution of sources towards higher altitude and wider vertical dispersion, while it does not change the proportion of backward trajectories meeting a cloud.

There is a pronounced seasonal cycle of the monthly average upward mass flux across the 380 K surface, with a maximum in February and a minimum in September, which is shifted by about month to the seasonal cycle of sources, due to the mean time of transit of parcels across the TTL.

The forward transit times are on the average of one month with a significant standard deviation of about 15 days but over continental Asia during summer where they are shorter (3 weeks from Asia Mainland (AML) and two weeks for Tibet). The backward transit times are longer and this discrepancy culminates for Tibet.

One of the main motivation of this study was to study how air parcels detrained from clouds find their way across the LZRH. Our results however show that the sources are mostly located above the LZRH, but not far, for about 80 %. This implies that only the small percentage of convective events penetrating high enough in the TTL is relevant

ACPD
15, 26231–26271, 2015

as stratospheric source. The proximity of sources to the LZRH is providing evidence that the vertical flow separation at this level is an important factor to determine the distribution of the sources. This will further demonstrated in a companion paper.

The high contribution of the tallest clouds rise a concern about the lack of representation of small-scale convective features in the CLAUS dataset and in the ERA-Interim heating rates. In particular, CLAUS captures very well the large anvils that form at the top of convective systems but misses the short and elusive overshooting events over these anvils. The velocities and radiative heating rates from reanalysis also miss the cross isentropic mixing provided by such event or represent them with very crude parameterisations.

Our study corroborates the special role of the Tibetan plateau in providing air to the Asian Monsoon anticyclone (AMA). We find that 87 % of the AMA air originates from continental Asia which agrees very well with the finding of Heath and Fuelberg (2014) (90 %), but our results differ from these authors by giving a much stronger weight to the Asian continental regions outside Tibet (AML). We find, however, that this proportion is sensitive to the representation of cloud tops and that it varies a lot within the literature: Fu et al. (2006) and Wright and Fueglistaler (2013) find like Heath and Fuelberg (2014) a prevalent role of Tibet while Aschmann et al. (2009) and Devasthale and Fueglistaler (2010) meet out conclusions. Nevertheless, Tibet is characterized by a very high efficiency at carrying air from the top of the clouds to the 380 K surface and short transit times. This provide a hint that Tibet is a sensitive area for increase of air pollution as boundary layer compounds processed by convection can be carried efficiently and rapidly to the stratosphere.

It remains that Tibet is an overall small contributor to the global transport into the stratosphere because most of the air entering the stratosphere during summer is not processed inside the AMA but is transported around, separating the location of convective from the entry point into the stratosphere (Bannister et al., 2004; James et al., 2008; Park et al., 2009).

ACPD
15, 26231–26271, 2015

Our results can be compared with those of Chen et al. (2012) and Orbe et al. (2015). Chen et al. (2012) uses kinematic trajectories from the boundary layer focusing on the summer season while Orbe et al. (2015) analyses impulse tracers transported by a general circulation model and provides a whole year analysis. Although both use a different set of regions within the tropics, our results regarding the regional distribution of sources and their seasonal variations are basically consistent with these two studies. There are discrepancies, however, in the transit time scales. Chen et al. (2012) shows a distribution of transit times from the boundary layer to the stratosphere which has a strong modal peak over Asia at about 3 days while, on the contrary, Orbe et al. (2015) shows a distribution which peaks at about two months. Our results lay somewhat between but such a discrepancy creates an issue that needs to be solved as transit times are an important necessary ingredient to understand and model the behaviour of many short live chemical species in the TTL and the lower stratosphere.

In spite of displaying the highest cloud tops (Liu and Zipser, 2005), the continental convection above Africa (Af) and South America (SAm) is a much weaker provider than the oceanic convection of SAP and North Asian Pacific Ocean (NAPO). However, our conclusions do not account for the effect of small-scale overshoots which are more commonly observed over these regions than over the oceans (Corti et al., 2008; Liu et al., 2010) due to the larger available convective energy.

Acknowledgements. These results were obtained using the CLAUS archive held at the British Atmospheric Data Centre, produced using ISCCP source data distributed by the NASA Langley Data Center. We acknowledge support from the EU 7th Framework Program under grant 603557 “StratoClim”.

References

Abalos, M., Randel, W. J., and Serrano, E.: Variability in upwelling across the tropical tropopause and correlations with tracers in the lower stratosphere, Atmos. Chem. Phys., 12, 11505–11517, doi:10.5194/acp-12-11505-2012, 2012. 26245

ACPD
15, 26231–26271, 2015

Adler, R. F. and Mack, R. A.: Thunderstorm Cloud Top Dynamics as Inferred from Satellite Observations and a Cloud Top Parcel Model, J. Atmos. Sci., 43, 1945–1960, doi:10.1175/1520-0469(1986)043<1945:TCTDAI>2.0.CO;2, 1986. 26235

Andrews, D. G., Holton, J. R., and Leovy, C. B.: Middle atmosphere dynamics, no. v. 40 in International geophysics series, Academic Press, Orlando, 1987. 26245

Appenzeller, C., Holton, J. R., and Rosenlof, K. H.: Seasonal variation of mass transport across the tropopause, J. Geophys. Res., 101, 15071–15071, doi:10.1029/96JD00821, 1996. 26245, 26246

Aschmann, J., Sinnhuber, B.-M., Atlas, E. L., and Schauffler, S. M.: Modeling the transport of very short-lived substances into the tropical upper troposphere and lower stratosphere, Atmos. Chem. Phys., 9, 9237–9247, doi:10.5194/acp-9-9237-2009, 2009. 26233, 26250

Bannister, R., O'Neill, A., Gregory, A., and Nissen, K.: The role of the south-east Asian monsoon and other seasonal features in creating the "tape-recorder" signal in the Unified Model, Q. J. Roy. Meteorol. Soc., 130, 1531–1554, doi:10.1256/qj.03.106, 2004. 26250

Bergman, J. W., Jensen, E. J., Pfister, L., and Yang, Q.: Seasonal differences of vertical-transport efficiency in the tropical tropopause layer: On the interplay between tropical deep convection, large-scale vertical ascent, and horizontal circulations, J. Geophys. Res., 117, D05302, doi:10.1029/2011JD016992, 2012. 26233

Bergman, J. W., Fierli, F., Jensen, E. J., Honomichl, S., and Pan, L. L.: Boundary layer sources for the Asian anticyclone: Regional contributions to a vertical conduit, J. Geophys. Res.-Atmos., 118, 2560–2575, doi:10.1002/jgrd.50142, 2013. 26233, 26239

Chen, B., Xu, X. D., Yang, S., and Zhao, T. L.: Climatological perspectives of air transport from atmospheric boundary layer to tropopause layer over Asian monsoon regions during boreal summer inferred from Lagrangian approach, Atmos. Chem. Phys., 12, 5827–5839, doi:10.5194/acp-12-5827-2012, 2012. 26233, 26251

Corti, T., Luo, B. P., Fu, Q., Vömel, H., and Peter, T.: The impact of cirrus clouds on tropical troposphere-to-stratosphere transport, Atmos. Chem. Phys., 6, 2539–2547, doi:10.5194/acp-6-2539-2006, 2006. 26232, 26233

Corti, T., Luo, B. P., de Reus, M., Brunner, D., Cairo, F., Mahoney, M. J., Martucci, G., Matthey, R., Mitev, V., dos Santos, F. H., Schiller, C., Shur, G., Sitnikov, N. M., Spelten, N., Vössing, H. J., Borrmann, S., and Peter, T.: Unprecedented evidence for deep convection hydrating the tropical stratosphere, Geophys. Res. Lett., 35, L10810, doi:10.1029/2008GL033641, 2008. 26251

ACPD
15, 26231–26271, 2015

Dee, D. P., Uppala, S. M., Simmons, A. J., Berrisford, P., Poli, P., Kobayashi, S., Andrae, U., Balmaseda, M. A., Balsamo, G., Bauer, P., Bechtold, P., Beljaars, A. C. M., Van de Berg, L. V. D., Bidlot, J., Bormann, N., Delsol, C., Dragani, R., Fuentes, M., Geer, A. J., Haimberger, L., Healy, S. B., Hersbach, H., Hólm, E. V., Isaksen, L., Kållberg, P., Köhler, M., Matricardi, M., McNally, A. P., Monge-Sanz, B. M., Morcrette, J. J., Park, B.-K., Peubey, C., de Rosnay, P., Tavolato, C., Thépaut, J.-N., and Vitart, F.: The ERA-Interim reanalysis: configuration and performance of the data assimilation system, Q. J. Roy. Meteorol. Soc., 137, 553–597, doi:10.1002/qj.828, 2011. 26234, 26235

Devasthale, A. and Fueglistaler, S.: A climatological perspective of deep convection penetrating the TTL during the Indian summer monsoon from the AVHRR and MODIS instruments, Atmos. Chem. Phys., 10, 4573–4582, doi:10.5194/acp-10-4573-2010, 2010. 26233, 26250

Folkins, I., Loewenstein, M., Podolske, J., Oltmans, S. J., and Proffitt, M.: A barrier to vertical mixing at 14 km in the tropics: Evidence from ozonesondes and aircraft measurements, J. Geophys. Res., 104, 22095–22095, doi:10.1029/1999JD900404, 1999. 26233

Fu, Q., Hu, Y., and Yang, Q.: Identifying the top of the tropical tropopause layer from vertical mass flux analysis and CALIPSO lidar cloud observations, Geophys. Res. Lett., 34, L14813, doi:10.1029/2007GL030099, 2007. 26232

Fu, R., Hu, Y., Wright, J. S., Jiang, J. H., Dickinson, R. E., Chen, M., Filipiak, M., Read, W. G., Waters, J. W., and Wu, D. L.: Short circuit of water vapor and polluted air to the global stratosphere by convective transport over the Tibetan Plateau, P. Natl. Acad. Sci. USA, 103, 5664–5669, doi:10.1073/pnas.0601584103, 2006. 26233, 26250

Fueglistaler, S., Wernli, H., and Peter, T.: Tropical troposphere-to-stratosphere transport inferred from trajectory calculations, J. Geophys. Res., 109, D03108, doi:10.1029/2003JD004069, 2004. 26233

Fueglistaler, S., Dessler, A. E., Dunkerton, T. J., Folkins, I., Fu, Q., and Mote, P. W.: Tropical tropopause layer, Rev. Geophys., 47, RG1004, doi:10.1029/2008RG000267, 2009. 26232

Gettelman, A., Salby, M. L., and Sassi, F.: Distribution and influence of convection in the tropical tropopause region, J. Geophys. Res., 107, 4080–4080, doi:10.1029/2001JD001048, 2002. 26233

Gettelman, A., Lauritzen, P. H., Park, M., and Kay, J. E.: Processes regulating short-lived species in the tropical tropopause layer, J. Geophys. Res., 114, D13303, doi:10.1029/2009JD011785, 2009. 26233

ACPD
15, 26231–26271, 2015

Hall, T. M. and Holzer, M.: Advective-diffusive mass flux and implications for stratosphere-troposphere exchange, Geophys. Res. Lett., 30, 1222, doi:10.1029/2002GL016419, 2003. 26244

Heath, N. K. and Fuelberg, H. E.: Using a WRF simulation to examine regions where convection impacts the Asian summer monsoon anticyclone, Atmos. Chem. Phys., 14, 2055–2070, doi:10.5194/acp-14-2055-2014, 2014. 26233, 26239, 26250

Highwood, E. J. and Hoskins, B. J.: The tropical tropopause, Q. J. Roy. Meteorol. Soc., 124, 1579–1604, doi:10.1002/qj.49712454911, 1998. 26232

Hodges, K. I., Chappell, D. W., Robinson, G. J., and Yang, G.: An improved algorithm for generating global window brightness temperatures from multiple satellite infrared imagery, J. Atmos. Ocean. Tech., 17, 1296–1312, 2000. 26234

Holton, J. R., Haynes, P. H., McIntyre, M. E., Douglass, A. R., Rood, R. B., and Pfister, L.: Stratosphere-troposphere exchange, Rev. Geophys., 33, 403, doi:10.1029/95RG02097, 1995. 26233, 26234

Holzer, M. and Hall, T. M.: Transit-Time and Tracer-Age Distributions in Geophysical Flows, J. Atmos. Sci., 57, 3539–3558, doi:10.1175/1520-0469(2000)057<3539:TTATAD>2.0.CO;2, 2000. 26238

James, R., Bonazzola, M., Legras, B., Surbled, K., and Fueglistaler, S.: Water vapor transport and dehydration above convective outflow during Asian monsoon, Geophys. Res. Lett., 35, L20810, doi:10.1029/2008GL035441, 2008. 26233, 26250

Kobayashi, S., Ota, Y., Harada, Y., Ebita, A., Moriya, M., Onoda, H., Onogi, K., Kamahori, H., Kobayashi, C., Endo, H., Miyaoka, K., and Takahashi, K.: The JRA-55 Reanalysis: General Specifications and Basic Characteristics, J. Meteorol. Soc. Jpn. Ser. II, 93, 5–48, doi:10.2151/jmsj.2015-001, 2015. 26243

Legras, B., Pisso, I., Berthet, G., and Lefèvre, F.: Variability of the Lagrangian turbulent diffusion in the lower stratosphere, Atmos. Chem. Phys., 5, 1605–1622, doi:10.5194/acp-5-1605-2005, 2005. 26238

Liu, C. and Zipser, E. J.: Global distribution of convection penetrating the tropical tropopause, J. Geophys. Res., 110, D23104, doi:10.1029/2005JD006063, 2005. 26232, 26251

Liu, X. M., Rivière, E. D., Marécal, V., Durry, G., Hamdouni, A., Arteta, J., and Khaykin, S.: Stratospheric water vapour budget and convection overshooting the tropopause: modelling study from SCOUT-AMMA, Atmos. Chem. Phys., 10, 8267–8286, doi:10.5194/acp-10-8267-2010, 2010. 26251

ACPD
15, 26231–26271, 2015

Luo, Z., Liu, G. Y., and Stephens, G. L.: CloudSat adding new insight into tropical penetrating convection, Geophys. Res. Lett., 35, L19819, doi:10.1029/2008GL035330, 2008. 26235
Minnis, P., Yost, C. R., Sun-Mack, S., and Chen, Y.: Estimating the top altitude of optically thick ice clouds from thermal infrared satellite observations using CALIPSO data, Geophys. Res. Lett., 35, L12801, doi:10.1029/2008GL033947, 2008. 26234
Orbe, C., Waugh, D. W., and Newman, P. A.: Air-mass origin in the tropical lower stratosphere: The influence of Asian boundary layer air, Geophys. Res. Lett., 42, 4240–4248, doi:10.1002/2015GL063937, 2015. 26233, 26251
Park, M., Randel, W. J., Gettelman, A., Massie, S. T., and Jiang, J. H.: Transport above the Asian summer monsoon anticyclone inferred from Aura Microwave Limb Sounder tracers, J. Geophys. Res., 112, D16309, doi:10.1029/2006JD008294, 2007. 26239
Park, M., Randel, W. J., Emmons, L. K., and Livesey, N. J.: Transport pathways of carbon monoxide in the Asian summer monsoon diagnosed from Model of Ozone and Related Tracers (MOZART), J. Geophys. Res., 114, D08303, doi:10.1029/2008JD010621, 2009. 26233, 26239, 26250
Pisso, I. and Legras, B.: Turbulent vertical diffusivity in the sub-tropical stratosphere, Atmos. Chem. Phys., 8, 697–707, doi:10.5194/acp-8-697-2008, 2008. 26235
Ploeger, F., Konopka, P., Müller, R., Fueglistaler, S., Schmidt, T., Manners, J. C., Grooß, J.-U., Günther, G., Forster, P. M., and Riese, M.: Horizontal transport affecting trace gas seasonality in the Tropical Tropopause Layer (TTL), J. Geophys. Res., 117, D09303, doi:10.1029/2011JD017267, 2012. 26233, 26248
Podglajen, A., Hertzog, A., Plougonven, R., and Žagar, N.: Assessment of the accuracy of (re)analyses in the equatorial lower stratosphere, J. Geophys. Res.-Atmos., 119, 11166–11188, doi:10.1002/2014JD021849, 2014. 26243
Sherwood, S. C., Chae, J.-H., Minnis, P., and McGill, M.: Underestimation of deep convective cloud tops by thermal imagery, Geophys. Res. Lett., 31, L11102, doi:10.1029/2004GL019699, 2004. 26234, 26235
Shine, K.: Sources and sinks of zonal momentum in the middle atmosphere diagnosed using the diabatic circulation, Q. J. Roy. Meteorol. Soc., 115, 265–292, doi:10.1002/qj.49711548604, 1989. 26246
Stohl, A., Forster, C., Frank, A., Seibert, P., and Wotawa, G.: Technical note: The Lagrangian particle dispersion model FLEXPART version 6.2, Atmos. Chem. Phys., 5, 2461–2474, doi:10.5194/acp-5-2461-2005, 2005. 26235

ACPD
15, 26231–26271, 2015

Tzella, A. and Legras, B.: A Lagrangian view of convective sources for transport of air across the Tropical Tropopause Layer: distribution, times and the radiative influence of clouds, Atmos. Chem. Phys., 11, 12517–12534, doi:10.5194/acp-11-12517-2011, 2011. 26233, 26235, 26239, 26240

Wright, J. S. and Fueglistaler, S.: Large differences in reanalyses of diabatic heating in the tropical upper troposphere and lower stratosphere, Atmos. Chem. Phys., 13, 9565–9576, doi:10.5194/acp-13-9565-2013, 2013. 26243, 26250

ACPD
15, 26231–26271, 2015

Table 1. Characteristic numbers of the vertical distribution of sources for the contributing regions during winter (DJF) and summer (JJA). All the quantities but the last column are in K. The modal peak is based on the discretized mean histogram shown in Fig. 3. The mean, median and standard deviation are calculated from a cubic spline interpolation over the 340–380 K interval. For each region and each season the upper line refers to backward calculations and the lower line to forward calculations as indicated in the modal peak column. The regions with low contribution have been masked.

Season	Region	LZRH	Modal peak	Mean	Median	Std dev	% above LZRH
DJF	Af	353.4	355 (B)	358.1	356.8	6.3	75.8
			355 (F)	359.5	357.9	6.8	82.5
	SAP	352.6	355 (B)	356.1	355.1	5.2	76.3
			355 (F)	358.7	357.3	5.9	89.5
	SAm	353.6	353 (B)	357.8	356.2	6.8	69.2
			355 (F)	358.7	357.4	6.4	77.1
JJA	Af	355.7	361 (B)	362.7	362	7.2	83
			359 (F)	363.1	362.2	7.2	83.7
	SAP	352.1	351 (B)	354.5	353.3	5.3	62
			353 (F)	356	354.9	5.5	75.3
	AML	359	361 (B)	363.1	362.5	5.7	75.4
			363 (F)	364.9	364.2	5.7	85.9
	NAPO	352.6	357 (B)	358.5	357.7	6.2	83
			359 (F)	360.5	359.6	6.5	90.7
	Tibet	367.3	363 (B)	365.4	364.7	5.2	31.4
			367 (F)	367.9	367.4	4.5	50.8
	NCP	351.3	351 (B)	353.8	352.4	5.5	62
			353 (F)	355.7	354.5	5.6	80
	CAm	350.7	353 (B)	357.4	355.5	7.4	82.5
			353 (F)	358	356.3	6.8	90.3

ACPD
15, 26231–26271, 2015

Table 2. Characteristic numbers of the distribution of transit times for the contributing regions during winter (DJF) and summer (JJA). All the quantities are in day. The modal peak is based on the discretized mean histogram shown in Fig. 4. The mean, median and standard deviation are calculated from a cubic spline interpolation over the 0–90 day interval. For each region and each season the upper line refers to backward calculations and the lower line to forward calculations as indicated in the modal peak column. The regions with low contribution have been masked.

Season	Region	Modal peak	Mean	Median	Std dev
DJF	Af	26 (B)	36.9	33.6	19.4
		26 (F)	27.5	25.7	14.6
	SAP	22 (B)	34.2	30.8	19.0
		18 (F)	23.4	20.6	13.3
	SAm	30 (B)	36.7	33.7	19.5
		26 (F)	28.2	26.5	14.4
JJA	Af	30 (B)	35.4	32.7	20.0
		26 (F)	29.5	27.8	16.9
	SAP	22 (B)	38.0	33.8	19.7
		22 (F)	30.9	27.6	15.3
	AML	26 (B)	32.5	29.4	19.7
		18 (F)	21.3	19.2	13.7
	NAPO	30 (B)	38.7	35.7	19.6
		26 (F)	28.4	26.6	15.8
	Tibet	14 (B)	29.5	24.3	19.6
		10 (F)	15.1	13	9.8
	NCP	22 (B)	37.2	33.3	19.2
		22 (F)	31.4	28.5	15.3
	CAm	30 (B)	37.9	35.2	19.5
		30 (F)	32.2	30.2	15.9

ACPD
15, 26231–26271, 2015

Table 3. Ratio of transport efficiency between forward calculations without cloud top offset and with a +1 km cloud top offset. The ratio is averaged over DJF and JJA for the 2005–2008 period and all regions. The values for weakly contributing regions, excluded from Tables 1 and 2, are based on a small number of events and are in italic.

	Af	ITA	SAP	AML	NAPO	CAm	SAm	Tibet	IO	NCP	SEP
DJF	0.45	*0.38*	0.45	*0.33*	*0.37*	*0.42*	0.46	*0.62*	*0.41*	*0.43*	*0.34*
JJA	0.49	*0.43*	0.46	0.36	0.42	0.46	*0.45*	0.22	*0.34*	0.46	*0.34*

ACPD
15, 26231–26271, 2015

Table 4. Distribution of annual mass flux, averaged over 2005–2008, for all the regions (in %).

Af	ITA	SAP	AML	NAPO	CAm	SAm	Tibet	IO	NCP	SEP
10.8	2.4	39.2	8	18	7.5	6	0.8	1.2	5.9	0.2

ACPD
15, 26231–26271, 2015

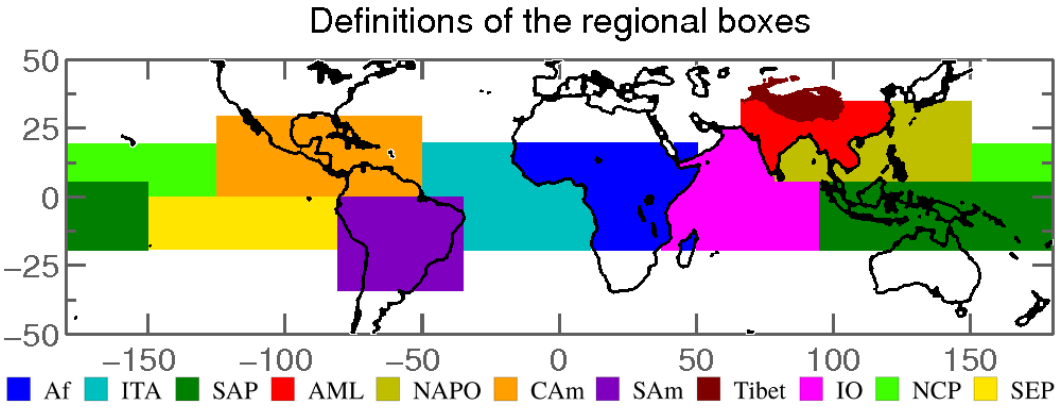

Figure 1. Distribution of the geographical regions within the tropics and the subtropics. In color, from west to east: North Central Pacific (NCP), South East Pacific (SEP), Central America (CAm), South America (SAm), Inter Tropical Atlantic (ITA), Africa (Af), Indian Ocean (IO), Asia Mainland (AML), Tibetan plateau (Tibet), North Asian-Pacific Ocean (NAPO) and South Asian Pacific (SAP). Tibet is defined as the region in Asia above 3500 m.

ACPD
15, 26231–26271, 2015

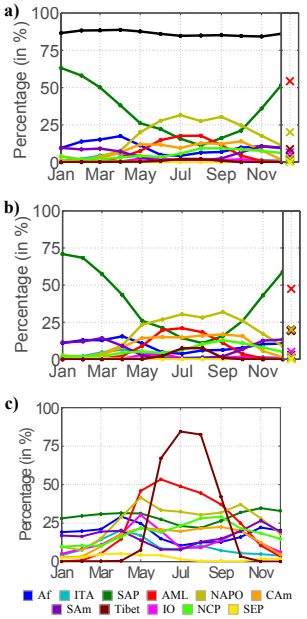

Figure 2. (a) Source distribution from backward calculations, calculated as the proportion of backward trajectories reaching a convective top within a given region among all trajectories reaching a convective top. Black line: proportion of backward trajectories reaching a convective top. **(b)** Source distribution from forward calculations, calculated as the proportion of forward trajectories reaching the tropopause from a given region among all the trajectories reaching the tropopause. **(c)** Efficiency of transport from convective tops, calculated as the proportion of parcels released in a given region that reach the tropopause in the forward calculations. On the right of **(a)** and **(b)** Source distribution for the inside of the Asian Monsoon Anticyclone averaged over JJA. The statistics are obtained for the period 2005–2008. The time axis refers to the instant grouped by months where a parcel leaves (forward) or meets (backward) a cloud but for the black curve in panel **(a)** for which the time axis is that of the launch of the parcels on the 380 K surface. Curves are plotted for each region, with the color code of Fig. 1.

ACPD
15, 26231–26271, 2015

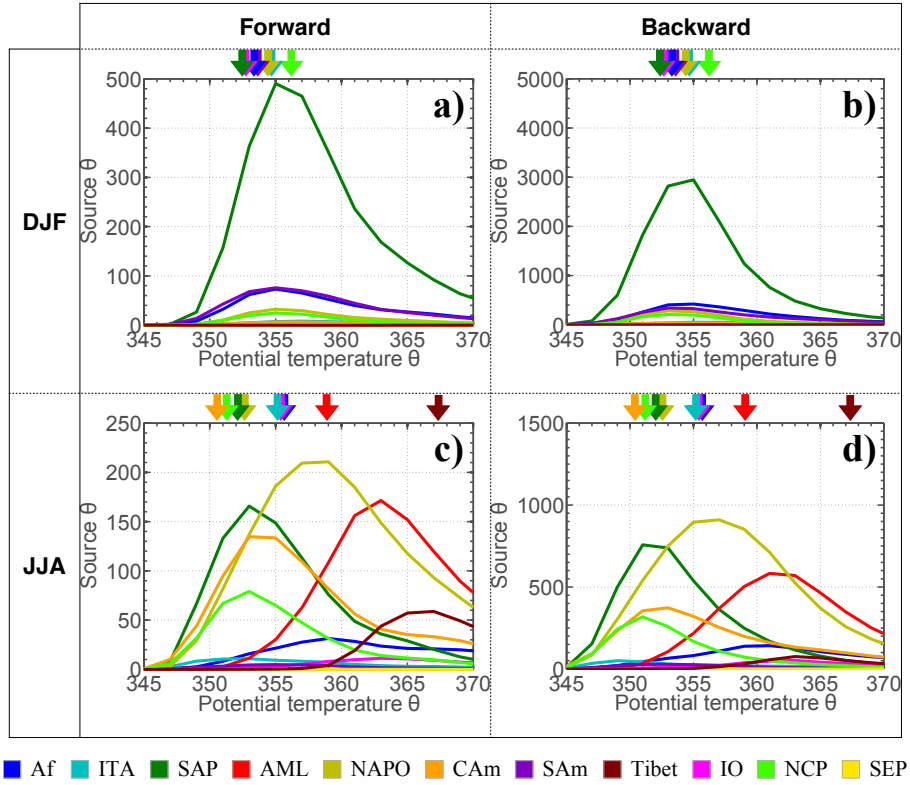

Figure 3. Vertical source distribution of the parcels in winter (DJF) and summer (JJA) for forward and backward calculations as a function of potential temperature of the source. The vertical axis counts the number of parcels calculated as monthly averages (then averaged over DJF and JJA and over 2005–2008) and are given in $K^{-1}\,day^{-1}$. Curves are plotted for each region, with the color code of Fig. 1. The arrows on the upper axes indicate the corresponding LZRH levels.

ACPD
15, 26231–26271, 2015

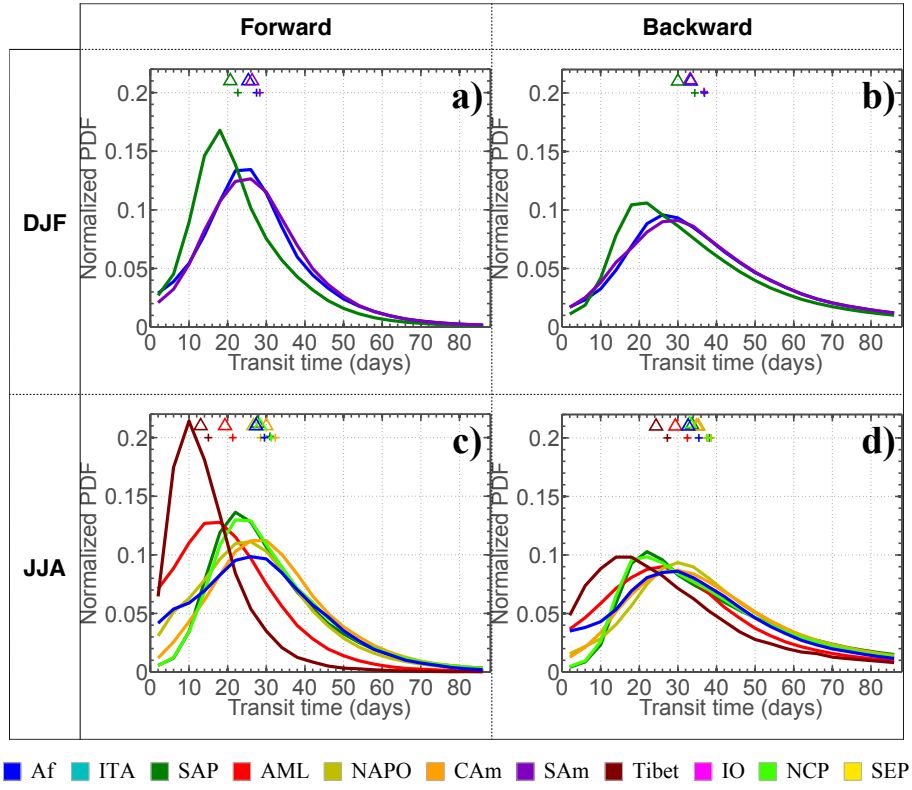

Figure 4. Distribution of the transit times in winter (DJF) and summer (JJA) for forward and backward calculations. The vertical axis is a normalized probability density function in day^{-1}. Curves are plotted according to the color code of Fig. 1 but only for the active convective regions during each season. In the upper part of each panel, the triangles and the crosses indicate, respectively, the median and the mean for each curve.

ACPD
15, 26231–26271, 2015

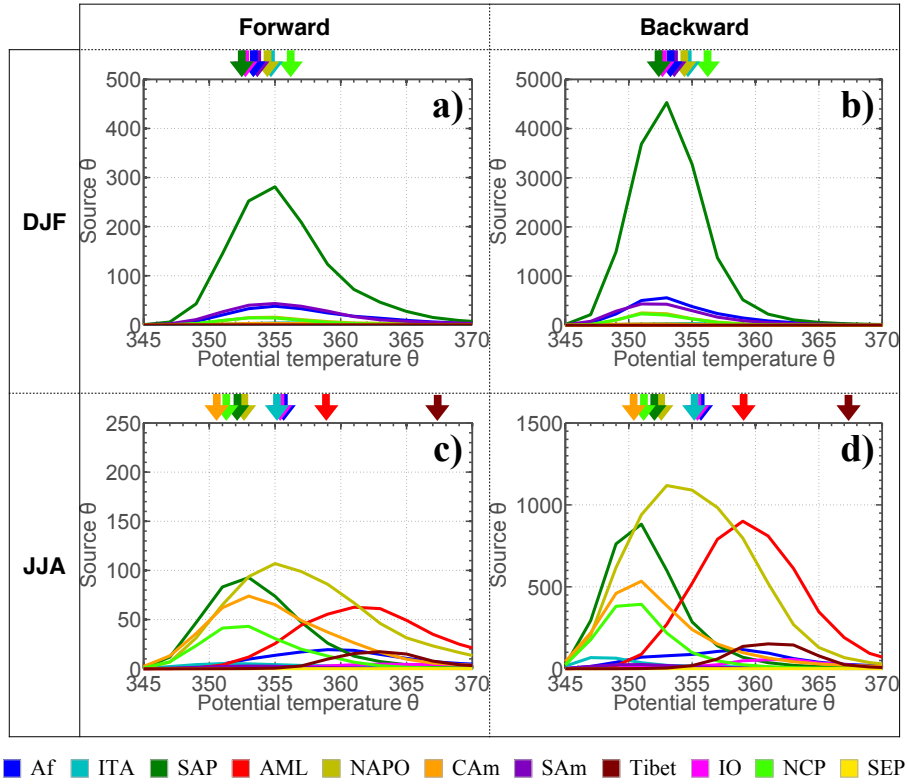

Figure 5. Same as Fig. 3 when the +1 km altitude correction of the cloud tops is not applied.

ACPD
15, 26231–26271, 2015

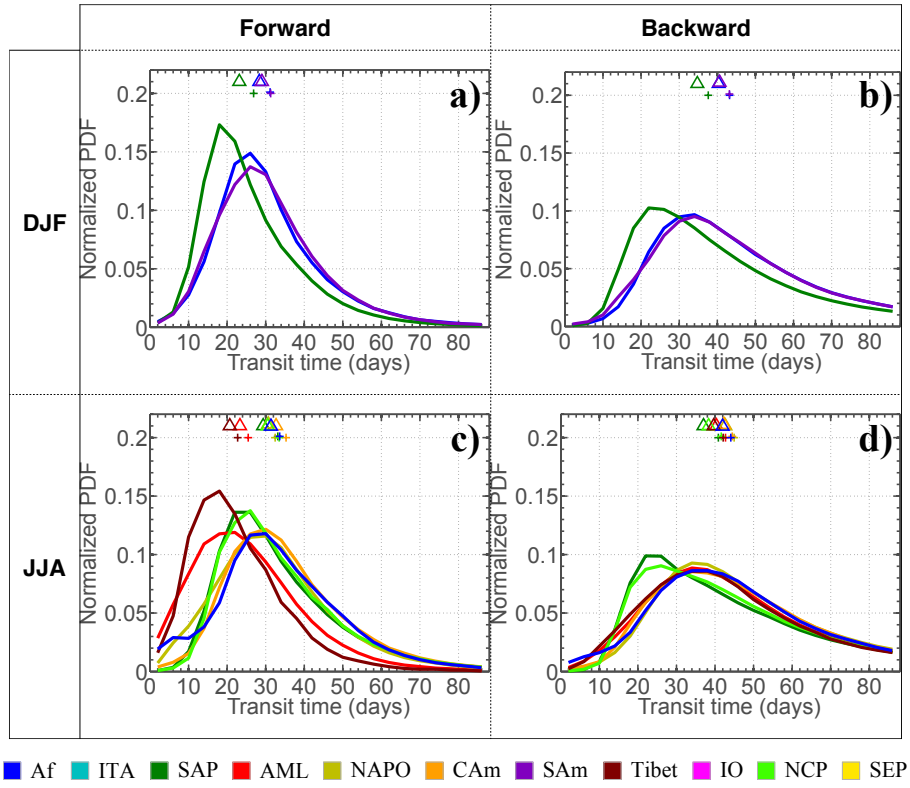

Figure 6. Same as Fig. 4 when the +1 km altitude correction of the cloud tops is not applied.

ACPD
15, 26231–26271, 2015

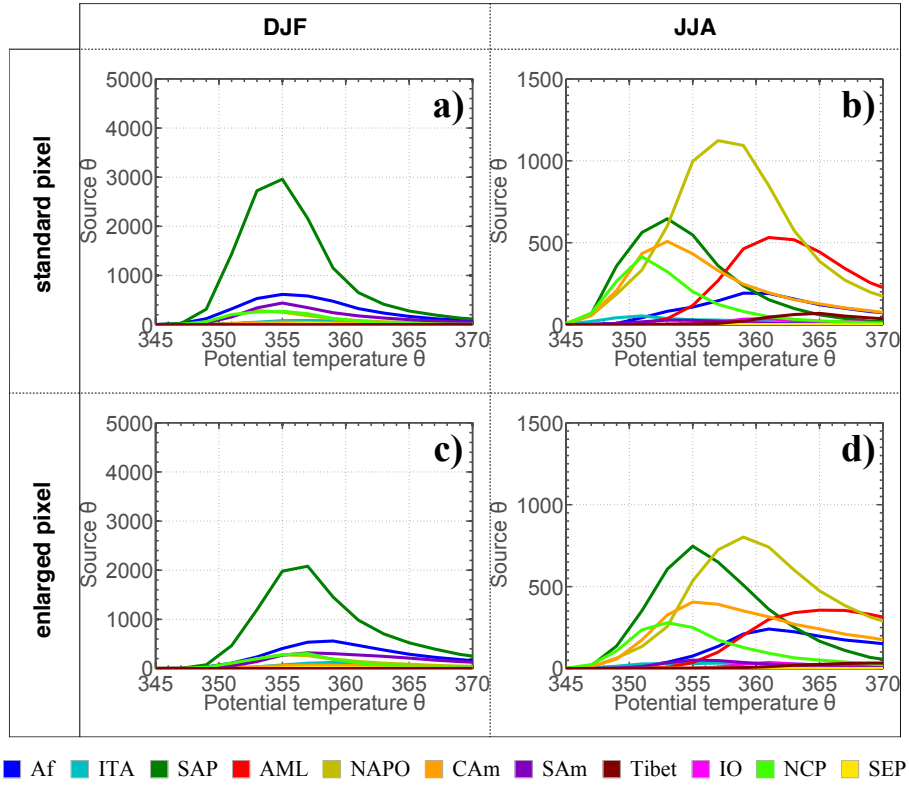

Figure 7. Comparison of the vertical source distribution for winter (DJF) and summer (JJA) between the standard backward calculation for 2005 (upper two panels) and when the CLAUS pixel size is enlarged by a factor 3 as described in the text (lower two panels).

ACPD
15, 26231–26271, 2015

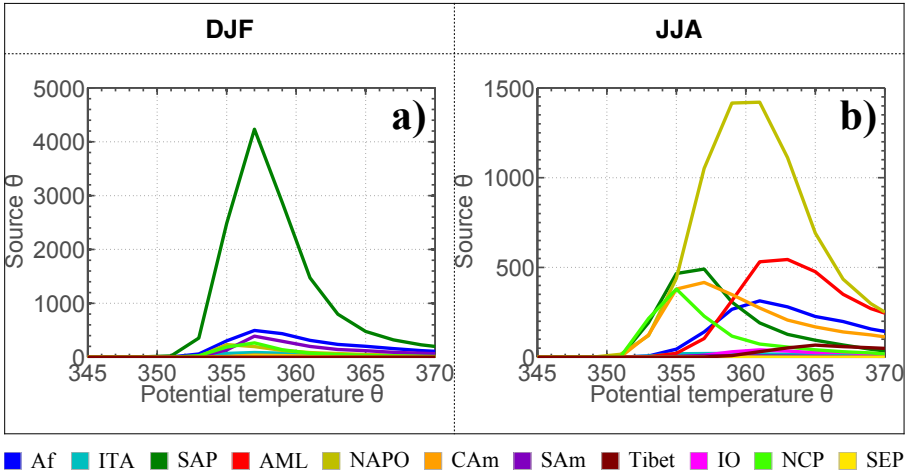

Figure 8. Vertical source distribution for winter (DJF) and summer (JJA) calculated for 2005 with JRA-55 reanalysis using the same setup as for ERA-Interim. This is to be compared with the two upper panels of Fig. 7.

ACPD
15, 26231–26271, 2015

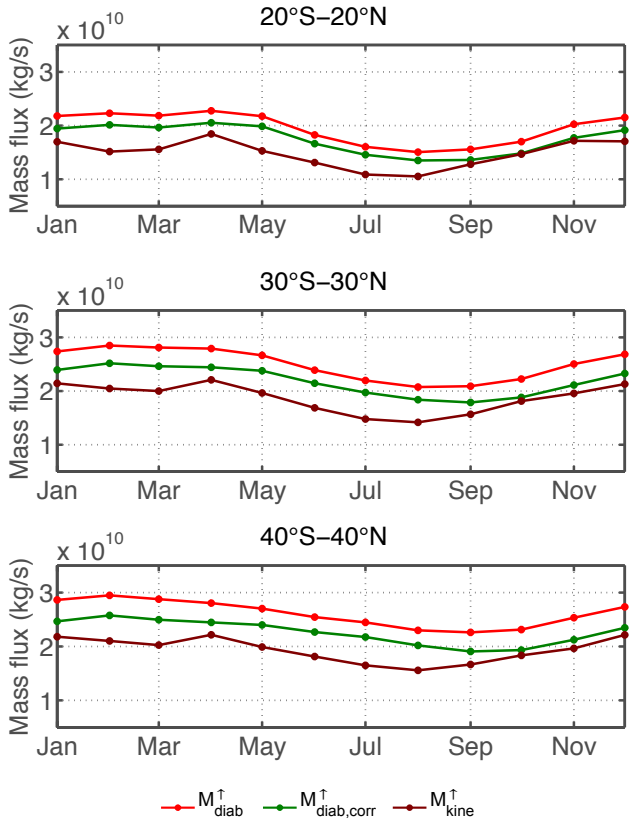

Figure 9. Annual variations of the monthly upward mass flux at the 380 K surface, calculated from the ERA-Interim data. $M^{\uparrow}_{\mathrm{diab}}$ and $M^{\uparrow}_{\mathrm{diab,corr}}$: diabatic mass flux calculated from the radiative heating rates of ERA-Interim respectively with and without the mass conservation correction of the radiative heating rates. $M^{\uparrow}_{\mathrm{kine}}$: kinematic mass flux calculated from the residual mean meridional circulation. All quantities are calculated and averaged over the years 2005 to 2008.

ACPD
15, 26231–26271, 2015

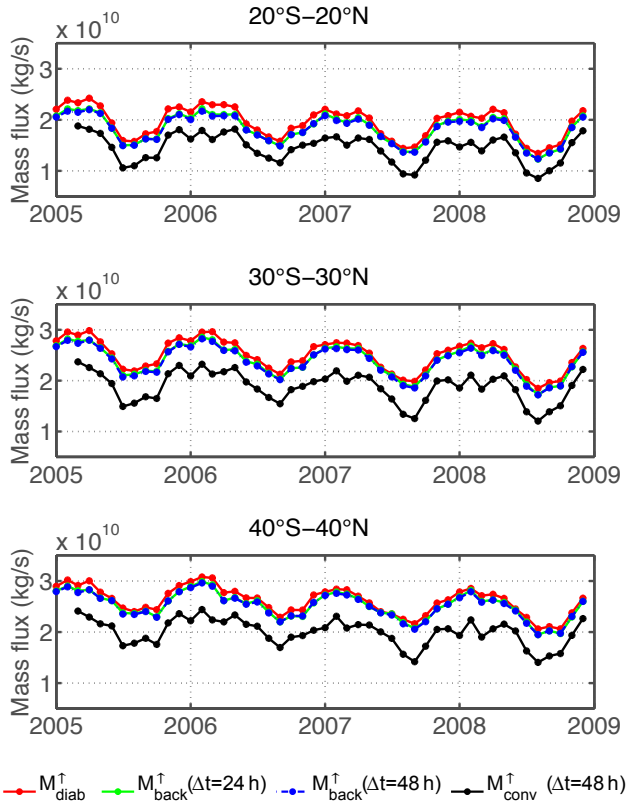

Figure 10. Uncorrected upward diabatic mass flux on the 380 K surface. $M^{\uparrow}_{\mathrm{diab}}$ (red) versus the Lagrangian diabatic mass flux $M^{\uparrow}_{\mathrm{back}}$ on the same surface calculated with delays $\Delta t = 24$ h (green) and $\Delta t = 48$ h (blue). The black curve shows $M^{\uparrow}_{\mathrm{conv}}$, that it the part of $M^{\uparrow}_{\mathrm{back}}$ with $\Delta t = 48$ h which originates from backward trajectories encountering a cloud within the previous 3 months.

ACPD
15, 26231–26271, 2015

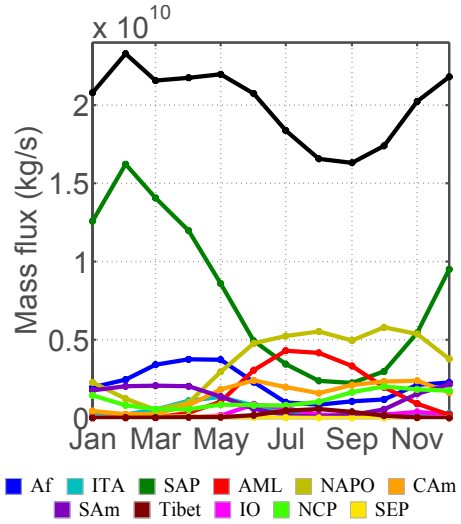

Figure 11. Distribution of the monthly upward mass flux at the 380 K within the band 40° S–40° N among the regions calculated from backward trajectories over 2005–2008. The black curve shows $M^{\uparrow}_{\mathrm{conv}}$. The time axis is that of the launch on the 380 K surface.

ACPD
15, 26231–26271, 2015